Comparison of Magnetically Induced ELF Fields in Humans Computed by FDTD and Scalar Potential FD Codes

Trevor W. Dawson, Jan De Moerloose and Maria A. Stuchly
Department of Electrical and Computer Engineering
University of Victoria
P.O. Box 3055, Victoria, British Columbia, Canada, V8W 3P6

Abstract

This paper presents a detailed numerical comparison, of the magnetically-induced extremely low-frequency electric field and current density within an anatomically realistic model of the full human body , as computed using two different numerical techniques.

The first technique is a recently-described full-wave quasi-static finite-difference time-domain (FDTD) method. The use of a time-ramped excitation involving pairs of oppositely-directed plane waves allows for the calculation of decoupled magnetic and electric induction in complex heterogeneous bodies, in relatively short (5 ns) simulation times.

The second method is an implementation of Stevenson's method applied for isolated conducting bodies. With the lowest-order external magnetic field represented by a vector potential, the lowest-order internal electric field can be represented by a scalar conduction potential, and the magnetically-induced contribution can be calculated in isolation.

Both methods have an underlying similarity in their finite-difference approach, but are nevertheless very distinct. Each code was used to calculate the fields, induced by three orthogonal uniform magnetic fields, in a 7.2 mm-resolution human full-body model. Three-dimensional correlation coefficients of better than 99.9998% were observed between current densities computed by the two methods. Individual edge electric fields typically agree to 3 significant digits.

1 Introduction

Accurate numerical modelling is an important component of the assessment of any potentially detrimental health effects of power-frequency electromagnetic fields on humans, if such effects are related to the induced electric fields and currents in tissue. Two commonly-used [1] numerical techniques are the finite-difference time-domain (FDTD) [2] method, and the impedance method (IM) [3, 4, 5]. In this paper, numerical computations using a modified FDTD method [6] will be compared to those computed using a less well-known scalar potential finite difference (hereafter frequently abbreviated as SPFD) technique, for magnetic excitation in an anatomically realistic heterogeneous human full-body model.

Although standard finite-difference time-domain codes are powerful and general, their direct application to extremely low-frequency modelling can result in excessively long simulation times on account of the stability criterion. For linear structures, however, it has recently been demonstrated [6] that the use of a time-ramped excitation involving pairs of oppositely-directed plane waves, can lead to an FDTD method that yields ELF fields in complex heterogeneous conducting bodies, in relatively short (5 ns) simulation times. By choosing the incident polarization appropriately, it is possible to treat the electric and magnetic source cases in a decoupled manner, as is desirable in a quasi-static framework. When applied to a human full-body model, the numerical FDTD implementation was shown [6] to give results that were both self-consistent, and in good agreement with previously-published data, for both electric and magnetic excitation. Nevertheless, as with any numerical model, independent verification of the numerical results is of utmost importance.

Interior calculations for magnetic sources have commonly been carried out using the Impedance Method, in which physical electric currents are represented by fictitious loop currents driven by the electromotive forces associated with the time-varying magnetic flux. The method has some attractive features. It can handle complex heterogeneous conductors, and gives rise to a sparse, naturally-preconditioned matrix system with only 13 non-zero diagonals. For the case of a

magnetic source, the forcing terms are available directly from the source fields. Solutions can be obtained using iterative methods. There are some drawbacks, however. Although the IM can be modified to incorporate injected currents, the result is not a comfortable match — fictitious external faces must be added around each surface node to support the partial loop currents that comprise the true injected current, and there is indeterminacy in the representation of a single scalar injection current in terms of multiple loop currents. Moreover, the underlying system of equations can be shown to be highly over-determined and is therefore singular. Nevertheless, iterative solution methods such as successive over-relaxation can in practice converge [3, 4, 5] to one of many possible solutions, and the indeterminacy is removed in the differencing of fictitious loop currents to yield physical edge currents. Also, in the case of multiply-connected domains, the method must be modified [7] to allow for generalized loop currents around the boundaries of insulating inclusions, or else physically incorrect solutions can be obtained. This modification becomes particularly onerous in three-dimensional modelling, but is nevertheless of major importance in human body modelling — insulating cavities occur in the airways, cranial sinuses and nasopharyngeal cavities, and pockets of gas may occur in the digestive tract.

At extremely low frequencies (ELF), electromagnetic induction in compact isolated conducting bodies can be handled by a simpler and more attractive scalar potential method. The indeterminacy in the underlying equations is removed, and the result is a matrix system which is approximately a factor of six smaller than in the impedance method formulation of the same problem. In Stevenson's Method [8], the electromagnetic fields external and internal to the conductor can each be be expanded locally in a power series in frequency. The lowest-order internal electric field is proportional to frequency, and is driven by the static incident components of the (external) electric and magnetic fields. This results in a capacitive component associated with the surface charge density induced by the applied electric field, plus a system of eddy currents driven by the applied magnetic field. If a vector potential for the applied magnetic field is available, it is possible to express the internal electric field solely in terms of a static scalar electric conduction potential. This potential has two forcing terms, one associated with the external surface charges, and the other, which is distributed throughout the interior of the conductor, with the magnetically induced electromotive force. Again, as with the modified FDTD, it is possible to treat electric and magnetic sources in a decoupled manner. Since the method appears to be less well-known, a self-contained description is provided in Section 2.3. The correctness of Stevenson's Method can be illustrated by examining the low-frequency limit of canonical problems, such as Mie scattering of a plane wave [8] from a uniformly conducting sphere.

Section 3 presents comparisons, from calculations using the FDTD and SPFD methods, of the electric fields and current densities induced by three orthogonal uniform magnetic fields, in a human full-body model at 7.2 mm resolution. Full three-dimensional correlation coefficients of better than 0.999998 were observed between the current density distributions computed by the two methods. Individual edge electric fields typically agree to 3 significant digits. In a companion paper [9], further validation of the SPFD method results is provided by a comparison with an analytical solution for low-frequency magnetic induction in a equatorially-stratified sphere.

2 Description of the Methods

2.1 General Description

A three-dimensional domain is described in terms of Cartesian coordinates (x, y, z) with associated unit vectors $\{\hat{\boldsymbol{x}}, \hat{\boldsymbol{y}}, \hat{\boldsymbol{z}}\}$, so that a typical position vector is $\boldsymbol{r} = x\,\hat{\boldsymbol{x}} + y\,\hat{\boldsymbol{y}} + z\,\hat{\boldsymbol{z}}$. A compact body, having a maximum diameter L and electrical conductivity and permittivity distributions $\sigma(\boldsymbol{r})$ and $\varepsilon(\boldsymbol{r})$ respectively, is located in this domain, and subjected to incident time-harmonic electric and magnetic fields $\boldsymbol{E}^e(\boldsymbol{r})\,e^{+i\omega t}$ and $\boldsymbol{B}^e(\boldsymbol{r})\,e^{+i\omega t}$ of angular frequency ω.

It is assumed that the inducing frequency is sufficiently low (quasi-static) that the body is much smaller than both the free-space wavelength, $L \ll \lambda \equiv 2\pi/k_0 = 2\pi c/\omega$ and the skin depth, $L \ll \delta \equiv [\omega\mu_0\sigma(\boldsymbol{r})/2]^{-1/2}$, and that conduction currents completely dominate displacement currents, $\sigma(\boldsymbol{r}) \gg \omega\varepsilon(\boldsymbol{r})$. The permittivity distribution plays no further role in the present analysis. Since the body is non-magnetic, the magnetic permeability has its vacuum value $\mu_0 = 4\pi \times 10^{-7}$ Hm^{-1} everywhere. Under these quasi-static assumptions, it is known that the internal electric field is in quadrature with the applied fields [8].

The task is to compute the fields induced in the conductor by the applied fields. The solution will be considered using both the FDTD and SPFD methods. In both methods, the three-dimensional computational domain is discretized into a uniform set of elementary

parallelepipeds or voxels. Within each voxel the electrical properties are assumed constant. The electric fields are defined as a set of discrete vectors on a staggered array defined by the voxel edges [10], with field values defined at the edge centers. Representative vectors are depicted in Figure 1. Magnetic fields are defined on a

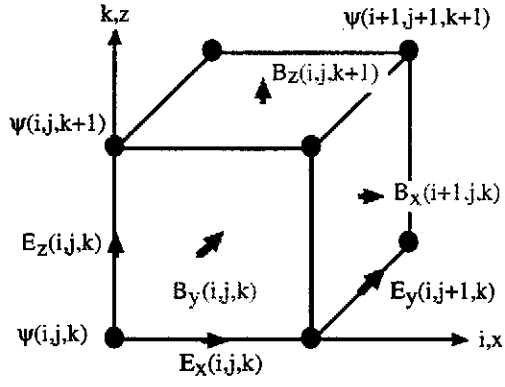

Figure 1: Representative discrete electric and magnetic field vectors, defined on conjugate staggered grids associated with the voxel edges and faces. The figure also illustrates representative discrete samples of the conduction potential, at the nodes defined by the voxel vertices.

conjugate mesh defined by the voxel face-normals.

In the full-wave FDTD method, the vector electric and magnetic fields are solved for directly, both interior and exterior to the conductor, by time-stepping. Absorbing boundaries are used to truncate the numerical mesh.

In contrast, the potential method is naturally confined only to the conductor (see Section 2.3), with potentials defined at the vertices of the voxels, as illustrated in Figure 1. It will be seen below that each discrete potential value is related to at most 6 others, so that the underlying matrix system has only 7 non-zero diagonals. Electric fields along the voxel edges are computed *a posteriori*, using finite differences of the potential field.

By way of comparison, it may be noted that the impedance method (which is also quasi-static) works with loop currents around the voxel faces, and so also is an intrinsically vector method. The final reduction of loop currents to physical edge currents yields the current density components along the voxel edges, as with the FDTD and SPFD methods. Each loop current is related to up to 12 others, leading to a matrix with 13 non-zero diagonals. Moreover, as it is a vector method, the number of unknowns is slightly more than 3 times as great.

The primary output of both the FDTD and SPFD codes is the set of discrete electric vector components. To allow for physical interpretation of the results, electric field vectors are defined at the voxel centers by averaging the three sets of four parallel edge components, and the current density is then computed by multiplication by the voxel conductivity.

For purposes of illustration, the methods will be applied to an anatomically realistic human full-body model, which is described in detail elsewhere [6]. It is a composite model, incorporating a Yale Medical School [11] head and torso model, augmented with legs and arms generated in our laboratory by the application of segmentation algorithms to CT and MRI data of the same man, obtained from the Visible Human Project at the U.S. National Library of Medicine. The tissue conductivities correspond to published [12], or where applicable, recently-measured [13], values. Particular care has been taken to ensure the correctness of the final model, verifying for example such items as continuity of major blood vessels and bone marrow, integrity of the skin, and encapsulation of bone marrow within bone, by visualization using IBM's Data Explorer program. The model provides a suitable complex heterogeneous domain for the rigorous comparison of numerical results. The original 3.6 mm resolution was decreased to 7.2 mm for this work. The end-result is described by a set of 213,782 cubic voxels with 7.2-mm edges. The model is oriented facing the $\hat{y}$ direction with the long axis of the body along the $\hat{z}$ direction. The source fields are taken to be uniform magnetic, at the 60-Hz power frequency.

2.2 FDTD Method

The finite-difference time-domain code is fully described and illustrated elsewhere [6]. This is a full-wave vector code, modified to take advantage of the fact that the phase of the external and internal fields is known in the quasi-static case. Indeed, fields exterior to the conductors all have the same phase as the incident field. Interior fields, however, are first-order fields in the quasi-static approximation and are proportional to the time derivative of the incident field. If a ramp function is used for the incident field, all fields will eventually have a linear (exterior) or constant (interior) behavior. The amplitude of the fields can then be read directly from their rate of change (exterior) or their actual values (interior). To obtain a solution, it is therefore sufficient to register all field values on two subsequent time steps after the transient response has decayed. The excitation function

used in this analysis is a ramp function with a smooth start to avoid high-frequency contamination. Absorbing boundary conditions [14] are used to truncate the numerical domain. On account of the retarded nature of any reflections and the short simulation times, these absorbing boundaries work well for low-frequency evanescent waves, even when placed close to the conductor. Another feature is that uniform electric and magnetic sources can be considered in isolation, by using oppositely-traveling plane waves with phases and polarizations adjusted to produce either uniform electric or magnetic source fields in the region of the conducting body.

2.3 SPFD Method

Under the present quasi-static assumptions, Stevenson's method [8] can also be applied. Each of the incident, scattered and interior electromagnetic fields can be expanded near the conductor in a power series involving the parameter $(-ik_0)$, where $k_0 = \omega/c$ denotes the vacuum wavenumber of the fields, and $c = (\varepsilon_0\mu_0)^{-1/2} \approx 2.998 \times 10^8\ \mathrm{ms}^{-1}$ is the vacuum speed of light. As explained by Van Bladel [8], the zeroth-order interior electric field in the series expansion is zero, and the interior magnetic field is equal to the zeroth-order applied magnetic field.

The first-order interior electric field has two sources. The first is the surface charge distribution $\rho_{s0}(\boldsymbol{r})$ induced by the zeroth-order applied electric field $\boldsymbol{E}_0^i(\boldsymbol{r})$. The second source is the applied zeroth-order external magnetic field $\boldsymbol{B}_0^e(\boldsymbol{r})$, which gives rise to the eddy currents that form the main focus of this work.

Mathematically, the first-order internal fields $\boldsymbol{E}_1^i(\boldsymbol{r})$ and $\boldsymbol{B}_1^i(\boldsymbol{r})$ satisfy the differential equations

$$\begin{aligned} \boldsymbol{\nabla} \times \boldsymbol{E}_1^i(\boldsymbol{r}) &= -i\omega \boldsymbol{B}_0^e(\boldsymbol{r}) \\ \boldsymbol{\nabla} \times \boldsymbol{B}_1^i(\boldsymbol{r}) &= \mu_0 \sigma(\boldsymbol{r})\, \boldsymbol{E}_1^i(\boldsymbol{r}) \end{aligned} \tag{2.1}$$

throughout the interior of the body. At its surface, where the outwardly-directed unit normal vector is $\hat{\boldsymbol{n}}(\boldsymbol{r})$, the appropriate boundary condition is

$$\sigma(\boldsymbol{r})\, \hat{\boldsymbol{n}}(\boldsymbol{r}) \cdot \boldsymbol{E}_1^i(\boldsymbol{r}) = i\omega \rho_{s0}(\boldsymbol{r}) . \tag{2.2}$$

Because of linearity, the contributions arising from the applied magnetic and surface charge forcing can be computed independently, by alternatively setting either the external magnetic field, or the surface charge density terms above to zero. The 'electric' contribution will be ignored for the remainder of this work, and the main focus will be on the internal electric field, and associated current density, generated by the magnetic source. The internal first-order magnetic field is strictly dependent on the internal electric field, and can be computed afterwards, if desired.

The problem, therefore, is to solve the differential equations

$$\begin{aligned} \boldsymbol{\nabla} \times \boldsymbol{E}_1^i(\boldsymbol{r}) &= -i\omega \boldsymbol{B}_0^e(\boldsymbol{r}) \\ \boldsymbol{\nabla} \cdot \left[\sigma(\boldsymbol{r})\, \boldsymbol{E}_1^i(\boldsymbol{r})\right] &= 0 \end{aligned} \tag{2.3}$$

(which are just the first member of equation (2.1) combined with the divergence of the second) within the body, subject to the boundary condition

$$\hat{\boldsymbol{n}}(\boldsymbol{r}) \cdot \boldsymbol{E}_1^i(\boldsymbol{r}) = 0 \tag{2.4}$$

at its surface. It is supposed that the static limit of the applied magnetic field can be described by a vector potential,

$$\boldsymbol{B}_0^e(\boldsymbol{r}) = \boldsymbol{\nabla} \times \boldsymbol{A}_0(\boldsymbol{r}) . \tag{2.5}$$

It then follows from equation (2.3) that

$$\boldsymbol{\nabla} \times \left\{ \boldsymbol{E}_1^i(\boldsymbol{r}) + i\omega \boldsymbol{A}_0(\boldsymbol{r}) \right\} = \boldsymbol{0}.$$

Consequently, the term in braces can be expressed as the negative gradient of a scalar potential $\psi(\boldsymbol{r})$, and the electric field has the representation

$$\boldsymbol{E}_1^i(\boldsymbol{r}) = -\boldsymbol{\nabla}\psi(\boldsymbol{r}) - i\omega \boldsymbol{A}_0(\boldsymbol{r}) . \tag{2.6}$$

This scalar potential must then satisfy the differential equation

$$\boldsymbol{\nabla} \cdot \left[\sigma(\boldsymbol{r})\, \boldsymbol{\nabla}\psi(\boldsymbol{r})\right] = \boldsymbol{\nabla} \cdot \left[-i\omega\sigma(\boldsymbol{r})\, \boldsymbol{A}_0(\boldsymbol{r})\right], \tag{2.7}$$

subject to the boundary condition

$$\hat{\boldsymbol{n}}(\boldsymbol{r}) \cdot \boldsymbol{\nabla}\psi(\boldsymbol{r}) = -i\omega \hat{\boldsymbol{n}}(\boldsymbol{r}) \cdot \boldsymbol{A}_0(\boldsymbol{r}) . \tag{2.8}$$

In a numerical implementation, the potential is taken to be defined at the voxel vertices. A finite-difference approximation for equation (2.7) at a given node can then be constructed by an application of the divergence theorem to an imaginary voxel with that node at its centre. It is convenient to adopt a local indexing scheme, where the target node is labeled 0 and both the nodes and edges connected to it on the $+x$, $-x$, $+y$, $-y$, $+z$ and $-z$ sides are indexed from 1 to 6 respectively, as shown in Figure 2. Quantities associated with nodes or edges are then labeled with the local index of the associated object. With this shorthand, a simple finite difference equation

$$\left(\sum_{r=1}^{6} s_r \right) \psi_0 - \sum_{r=1}^{6} s_r \psi_r = i\omega \sum_{r=1}^{6} (-1)^{r+1} s_r \ell_r A_{0r} \tag{2.9}$$

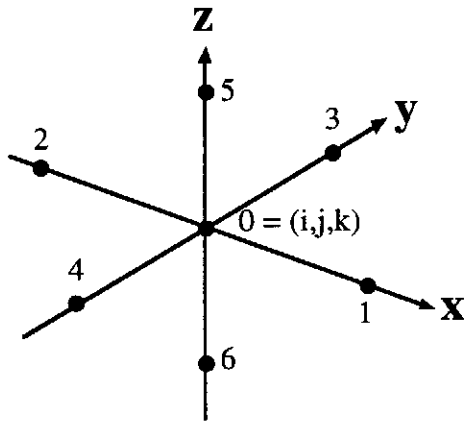

Figure 2: Local indexing scheme at a node.

results. In this equation, ℓ_r denote the various edge lengths in the local indexing scheme, and A_{0r} denotes the component of the external magnetic vector potential tangent to the r^{th} edge, evaluated at the edge centre. The coefficients are the edge conductances $s_r \equiv \bar{\sigma}_r a_r / \ell_r$, where $\bar{\sigma}_r$ denotes the average conductivity of the four voxels contacting edge r, a_r is the area of the voxel face normal to edge r. The above equations are to be modified in an obvious manner if the central point is connected to less than 6 neighbouring nodes in the conductor.

When this equation is written for each vertex of every conducting voxel in the distribution, the result is a heptadiagonal system of equations of the form $(N - E)\,y = f$. This set of equations is diagonally dominant, symmetric, positive semi-definite. It is also singular, since the potential is indeterminate to within an additive constant. It can be symmetrically preconditioned to the form $(I - A)\,x = b$, where $A = N^{-1/2} E N^{-1/2}$, $y = N^{-1/2} x$ and $b = N^{-1/2} f$. The singularity can be removed by augmenting the system with an equation requiring that the potential have zero mean. The net result of augmentation and preconditioning is a system, based on a symmetric sparse matrix with two borders, that is amenable to solution using the conjugate gradient iterative scheme.

3 Results

Results computed by the FDTD code for incident uniform magnetic field directed along the three Cartesian axes are described in detail elsewhere [6], and shown to be both self-consistent and in reasonable agreement with results computed by other methods. In these computations, the bounding box containing the body model was surrounded by a single-voxel air layer, and the whole surrounded on all sides by a 15-voxel thick absorbing boundary. Thus the calculations were performed over a $107 \times 77 \times 280$ array, for an overall domain composed of $2,306,920$ voxels. Each run employed 4200 time steps of 1.2 ps, for a total simulation time of 4.92 ns. All calculations were carried out on a Hewlett-Packard 9000/735 Unix workstation with 336 megabytes of physical memory. Typical computation times were of the order of 18 hours.

Results were also computed by the SPFD code, for the same body configuration and excitation fields. The resulting augmented and preconditioned potential matrix system consisted of $240,883$ unknowns, and was found to be reliably solvable using the Conjugate Gradient Method (CGM) [15] from the PIM [16] package, running in sequential mode on the above-mentioned workstation. Typical run times were of the order of 1 hour.

As noted earlier, electric fields and current densities were defined at voxel centers using edge-averaged electric fields. This leads to fields defined for every voxel in the $75 \times 45 \times 248$-voxel bounding box containing the body model, and the calculations can be compared voxel-by-voxel throughout the conducting voxels.

To illustrate the comparisons obtained, Figure 3 depicts the results in a horizontal (left-to-right, back-to-front) cross-section through the chest area (at a height $z = 1.357$ m above the lowest conducting voxel face) of the model, under induction by an x-directed (left-to-right) 1 μT uniform magnetic field. The upper left panel of the figure shows the magnitude of the electric field computed by the SPFD code, while the lower left panel shows the magnitude of the corresponding current density. The upper right panel shows the magnitude of the voxel-wise vector difference of the FDTD and SPFD electric fields, while the lower right panel displays the analogous difference of the current density. Particular attention is drawn to the approximately three orders of magnitude difference in scale between the electric field and the electric difference, and nearly four orders of magnitude for the corresponding current density plots.

Figure 4 shows a current density comparison along a vertical (back-to-front, groin-to-head) cross-section (at a distance $x = 26.28$ cm from the leftmost conducting voxel face), under forcing by a vertical magnetic field configuration.

To further quantify the agreement between results computed by the two methods, a set of scalar descriptors is provided in Table I. All measures are taken solely

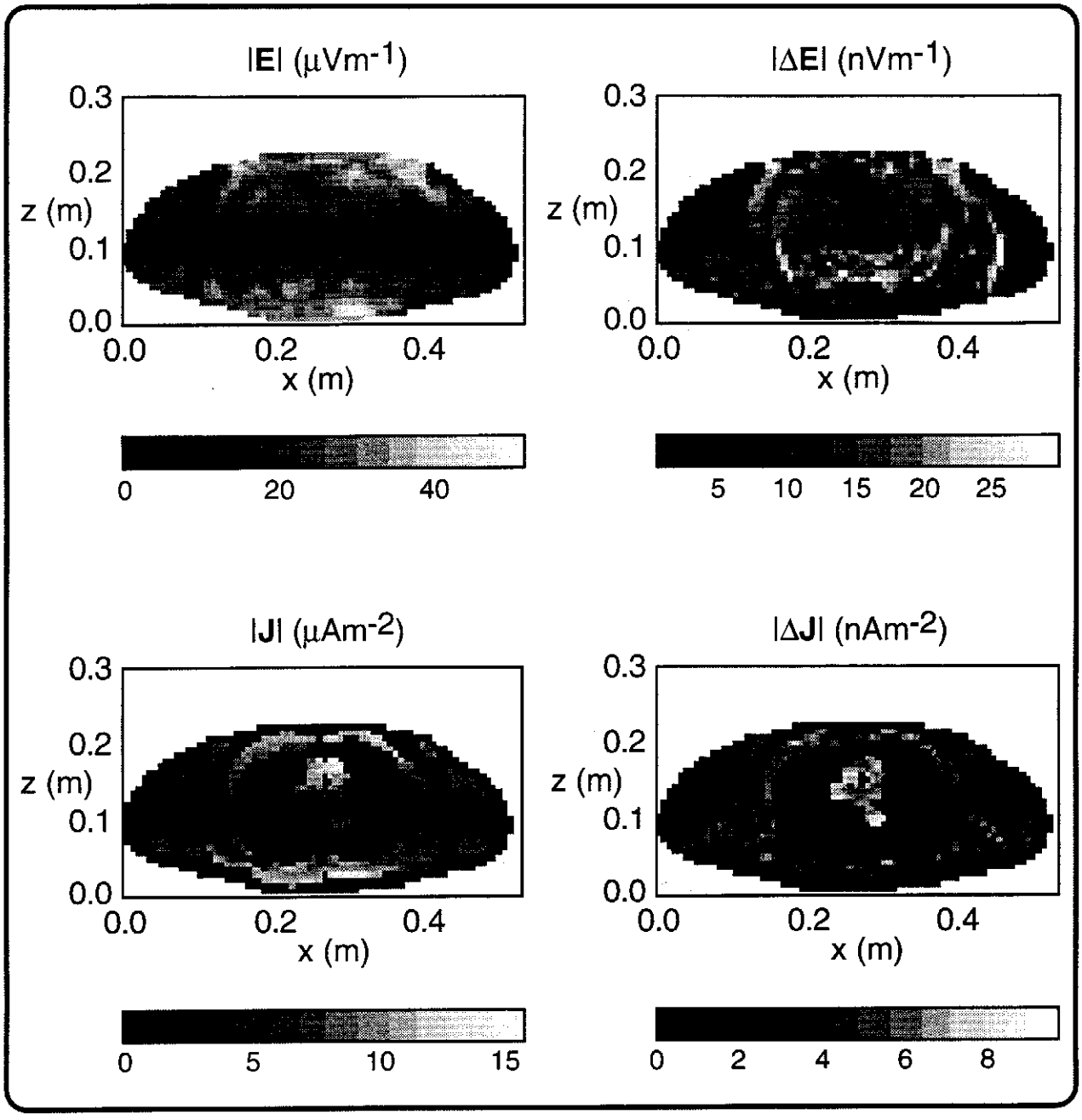

Figure 3: Comparison of the SPFD calculations (left-hand column) and voxel-wise differences between the FDTD and SPFD results (right-hand column) in a horizontal cross section through the chest. The 60-Hz, 1-μT magnetic source field is directed from left to right. The upper left panel depicts the magnitude of the electric field, while the upper right panel illustrated the magnitude of the vector difference. The lower row portrays analogous data for the current density. Note the factor of 1000 difference in units between the left- and right-hand units.

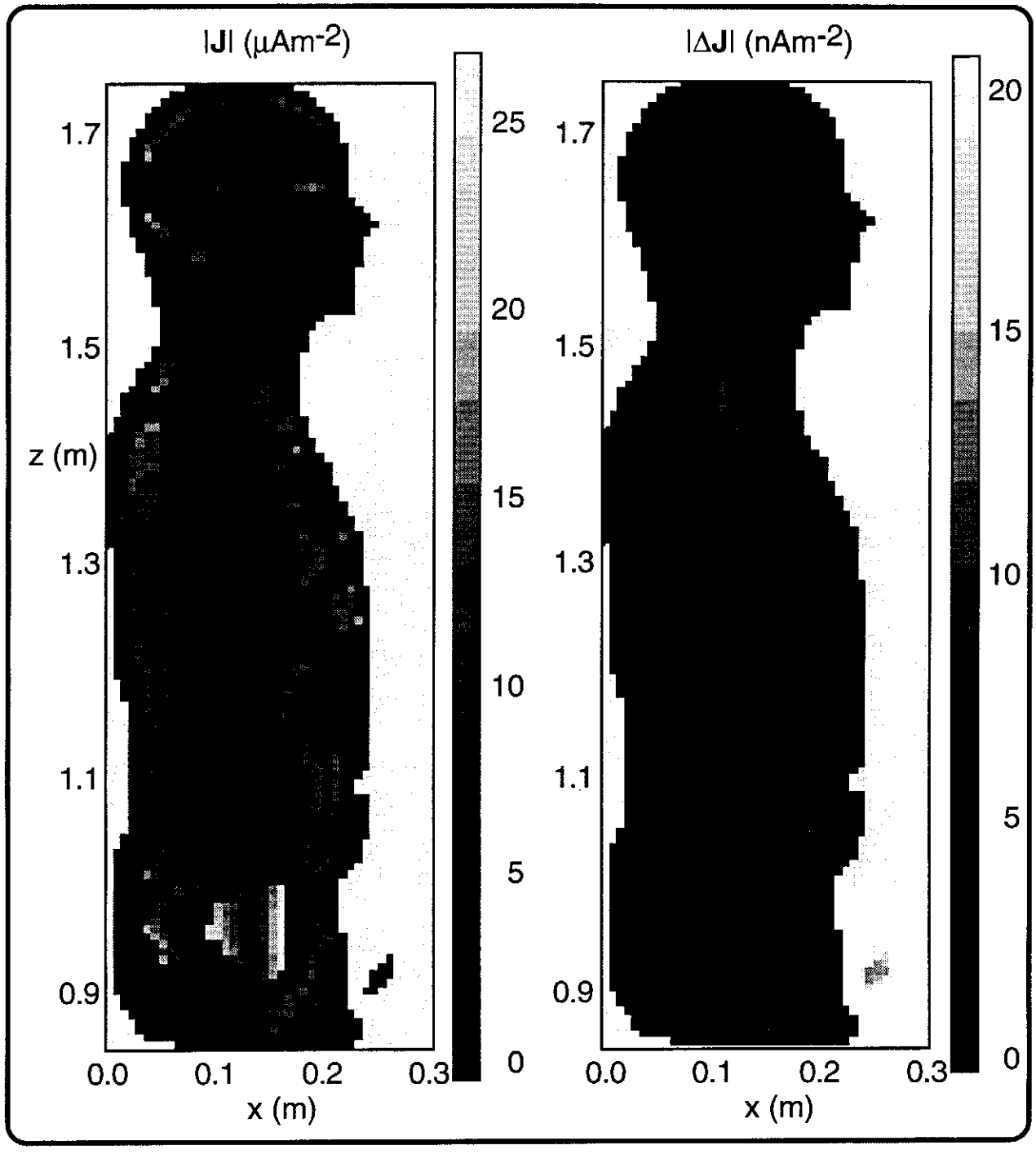

Figure 4: Comparison of the magnitudes of the current density (left) and difference (right) fields in a central vertical cross-section, for a vertical 60-Hz, 1-μT magnetic source field.

	Field :	$\lvert\mathbf{E}\rvert$ $(\mu\mathrm{Vm}^{-1})$			$\lvert\mathbf{J}\rvert$ $(\mu\mathrm{Am}^{-2})$		
	Source :	B_x	B_y	B_z	B_x	B_y	B_z
	Cor. (%)	99.05054	99.79887	99.63219	99.99997	99.99984	99.99998
FDTD	Maximum	123.0281	756.7335	104.7555	70.7892	75.6733	31.5956
	Average	15.0586	20.4341	13.3078	2.8565	3.9026	2.4186
	Std. Dev.	27.8941	39.1021	24.4372	5.7031	7.8438	4.7016
SPFD	Maximum	81.9336	758.5416	104.7452	70.7973	75.8542	31.5978
	Average	14.9101	20.3426	13.2235	2.8568	3.9021	2.4187
	Std. Dev.	27.6243	38.9712	24.3103	5.7037	7.8431	4.7018
Δ	Maximum	123.0281	83.9447	67.7967	0.0424	0.1736	0.0477
	Average	0.1484	0.0916	0.0842	−0.0003	0.0005	−0.0001
	Std. Dev.	2.5218	1.6959	1.3614	0.0033	0.0102	0.0019

Table I: Electric field and current density modulus comparisons for three orthogonal (left-to-right, back-to-front and foot-to-head) 1 μT uniform magnetic sources. The correlation coefficient for each field type relates the FDTD and SPFD calculations. The remaining rows show various scalar comparisons between the two calculated fields, plus measures of the voxel-wise difference between the fields computed by the two codes. All measures are taken solely over voxels belonging to the body model.

over voxels belonging to the body model, i.e. specifically excluding air cells external to the body. Scalar descriptors include the voxel-wise correlation between between the FDTD and SPFD fields. In addition, for each method, the global maximum and average values are tabulated, as well as the standard deviation. The latter is included purely as an indicator of the variation in a given field, *not* as a statistical measure. These indicators are tabulated for the FDTD results and for the SPFD computations, as well as to the difference (FDTD−SPFD) fields. These comparisons were performed for the magnitude of the electric field and current density distributions, under excitation by x-, y- and z-directed 60-Hz, 1-μT uniform magnetic source fields.

The electric field measured indicate a reasonable agreement between the methods, with the global measures (average and standard deviation) differing only in the third decimal place. The smallest electric field correlation coefficient is 99.05%, for the x-directed magnetic field. The peak field values for this excitation are also in poor agreement. On closer examination however, it turns out that these differences are entirely associated with the occurrence of non-conducting air and gas pockets within the body. The electric fields are not computed and are automatically set to zero within such non-conducting volumes in the numerical implementation of the SPFD method. In the FDTD method, however, fields are computed at all voxels in the computational domain. The physical interpretation of the fields within interior non-conducting regions in the quasi-static FDTD code has not yet been clarified.

As might then be expected and is verified by the figures, the additional order imposed by the incorporation of the conductivity distribution and its associated removal of any contributions from non-conducting cavities, dramatically improves the current density correlation coefficients (the smallest of which is now 99.9998%), as well as the overall agreement indicated by the various scalar measures. The peak values now differ in the third decimal place at worst, while the global measures differ in the fifth.

4 Conclusions

Two distinct numerical methods, namely a finite-difference time-domain code, and a static scalar potential finite-difference code, have been used to compute the magnetically-induced electric fields and current densities in an anatomically realistic heterogeneous human full-body model. With three orthogonal source orientations, the model provides a rigorous test of the methods and of the correctness of the computer coding.

In all cases, the minimum full-body three-dimensional voxel-wise correlation coefficient for the electric field magnitude was found to be 0.9905. The corresponding minimum for the current densities was 0.999998. A variety of other scalar measures verifies the high degree of agreement that was obtained using the two methods. Any significant electric field differences which do occur

are attributable to the presence of non-conducting cavities within the body, where the SPFD code does not presently compute electric fields. The agreement between the current density fields computed by the two codes is excellent.

While the resolution is still rather coarse for detailed organ dosimetry, and there is the possibility of appreciable staircasing errors introduced by the volumetric discretization, the agreement between the methods provides a degree of comfort in using results computed by either code.

Acknowledgment :

The authors thank Kris Caputa for his contribution to the development of the human body model, and the three anonymous reviewers for their suggested improvements to the paper. The financial support of this research by NSERC, B.C. Hydro, TransAlta Utilities and Ontario Hydro is gratefully acknowledged.

References

[1] Om P. Gandhi. Some numerical methods for dosimetry: Extremely low frequencies to microwave frequencies. *Radio Science*, **30**(1):161–177, January-February 1995.

[2] Om P. Gandhi and Jin-Yuang Chen. Numerical dosimetry at power-line frequencies using anatomically based models. *Biolelectromagnetics Supplement*, 1:43–60, 1992.

[3] Om. P. Gandhi, John F. DeFord, and Hiroshi Kanai. Impedance method for calculation of power deposition patterns in magnetically induced hyperthermia. *IEEE. Trans. Biomedical Engineering*, **BME-31**(10):644–651, October 1984.

[4] Niel Orcutt and Om P. Gandhi. A 3-D impedance method to calculate power deposition in biological bodies subjected to time varying magnetic fields. *IEEE. Trans. Biomedical Engineering*, **35**(8):577–583, August 1988.

[5] Weiguo Xi, Maria A. Stuchly, and Om P. Gandhi. Induced electric currents in models of man and rodents from 60 Hz magnetic fields. *IEEE Trans. Biomed. Eng.*, **BME-41**(11):1018–1023, 1994.

[6] Jan De Moerloose, Trevor W. Dawson, and Maria A. Stuchly. Application of FDTD to quasi-static field analysis. *Radio Science*, 1996. manuscript submitted for publication.

[7] Francis X. Hart, Kimberly Evely, and Carla D. Finch. Use of a spreadsheet program to calculate the electric field/current density distributions in irregularly shaped, inhomogeneous biological structures by low-frequency magnetic fields. *Bioelectromagnetics*, **14**:161–172, 1993.

[8] J. Van Bladel. *Electromagnetic Fields.* Hemisphere Publishing Corporation, Washington D.C., revised printing edition, 1985.

[9] Trevor W. Dawson and Maria A. Stuchly. Analytic validation of a three-dimensional scalar-potential finite-difference code for low-frequency magnetic induction. *Applied Computational Electromagnetics Society Journal*, 1996. manuscript accepted for publication.

[10] K.S. Yee. Numerical solutions to initial boundary value problem involving maxwell's equations in isotropic media. *IEEE Trans. Antennas Propag.*, **14**:302–307, 1966.

[11] I. G. Zubal, C. R. Harrell, E. O. Smith, Z. Rattner, G. R. Gindi, and P. H. Hoffer. Computerized three dimensional segmented human anatomy. *Med. Phys. Biol.*, **21**:299–302, 1994.

[12] K. R. Foster and H. P. Schwan. Dielectric properties of tissues and biological materials: a critical review. *CRC Critical Reviews in Biomedical Engineering*, **17**:25–104, 1989.

[13] Dr. C. Gabriel. Personal communication, 1996.

[14] J. P. Berenger. A perfectly matched layer for the absorption of electromagnetic waves. *J. Comp. Phys.*, **114**:185–200, 1994.

[15] John L. Volakis. EM programmer's notebook. *IEEE Antennas and Propagation Magazine*, **37**(6):94–96, 1995.

[16] R.D. da Cunha and T.R. Hopkins. PIM 2.0 : Parallel Iterative Methods package for systems of linear equations; (FORTRAN 77 version), 1993. ©1993 R.D. da Cunha, T.R. Hopkins and Computing Laboratory, University of Kent at Canterbury, Canterbury, U.K. and Centro de Processamento de Dados, Universidade Federal do Rio Grande do Sul, Porto Alegre, Brasil.